ELSEVIER

Journal of Structural Geology 28 (2006) 19–35

JOURNAL OF STRUCTURAL GEOLOGY

www.elsevier.com/locate/jsg

Double-edge fault-propagation folding: geometry and kinematics

S. Tavani *, F. Storti, F. Salvini

Dipartimento di Scienze Geologiche, Università degli Studi "Roma Tre" Largo S. L. Murialdo 1, 00146 Rome, Italy

Received 14 March 2005; received in revised form 3 August 2005; accepted 21 September 2005
Available online 2 November 2005

Abstract

Fault-propagation folding is a common folding mechanism in thrust-and-fold belts and accretionary prisms. Several geometrical models relating the fold shape to the ramp shape have been proposed. In all these models, ramps always emanate from a basal fault and propagate upwards. We have developed a new kinematic and geometric model of fault-propagation folding, named double-edge fault-propagation folding. The model simulates folding at thrust ramps as a function of their nucleation site and propagation history within the folded multilayer. The fold shape depends on the initial length and location of the ramp, its dip, and the *S*/*P* ratio (i.e. incremental ramp slip versus propagation) of both the upper and lower ramp tips. This solution increases the geometrical flexibility of fault-propagation folding reducing, for example, the direct dependence between the backlimb dip and the ramp dip, as double-edge fault-propagation folding is characterised by a backlimb panel not necessary parallel to the ramp. Non-parallelism between the ramp and the backlimb is commonly observed in thrust-related anticlines, within fold-and-thrust belts and accretionary prisms. The excess layer-parallel shear imposed by the development of double-edge fault-propagation folding can be easily accommodated by discrete faulting and/or penetrative deformation. The dependence of the fold shape on the fault behaviour provides a tool for including the role of mechanical stratigraphy and environmental conditions of deformation into kinematic models. Natural examples of anticlines that could be modelled by double-edge fault-propagation are presented.

Keywords: Fault-propagation folding; Kinematic model; Excess shear; Fault displacement; Fault *S*/*P* ratio

1. Introduction

Faults and folds in thrust-and-fold belts developing at shallow structural levels exhibit interdependences that have been largely investigated in the last decades (e.g. Rich, 1934; Bally et al., 1966; Dahlstrom, 1969; Elliott, 1976; Hossack, 1979; Suppe, 1983, 1985; Williams and Chapman, 1983; Price, 1988; Woodward et al., 1989, among others). In particular, folding ahead of upward propagating thrust ramps (tip-line folding; e.g. Dahlstrom, 1969; Elliott, 1976; Suppe and Medwedeff, 1984) has long been recognised as an efficient mechanism to accommodate fault displacement (e.g. Dahlstrom, 1969; Faill, 1973; Elliott, 1976; Williams and Chapman, 1983). Several geometric and kinematic models have been proposed for fault-propagation folding. In the simpler model configurations folds grow by flexural slip and no excess layer-parallel shear is predicted (Suppe, 1985; Chester and Chester, 1990; Suppe and Medwedeff, 1990; Mercier et al., 1997). These solutions imply a univocal fold interlimb angle for a given fault step-up angle. The range of possible fold shapes is significantly expanded in the case of either non-zero shear (e.g. Mosar and Suppe, 1992) or bed thickness variations (Jamison, 1987; Chester and Chester, 1990; Mitra, 1990; Suppe and Medwedeff, 1990; Wickham, 1995). In particular, only the cross-sectional area of the structure is preserved in trishear fault-propagation folding (Erslev, 1991; Hardy and Ford, 1997; Allmendinger, 1998; Cristallini and Allmendinger, 2002).

Despite the variety of kinematic and geometric solutions, available models of fault-propagation folding do not yet account for some key features that likely characterise the early evolutionary stages of many natural fault-related folds. Modern accretionary prisms provide the opportunity to place some basic constraints on fault–fold growth as imaged in reflection seismic profiles (e.g. Morgan and Karig, 1995). The first important feature occurring in embryonic structures and then preserved in the mature ones is the presence in the anticlinal backlimbs, of sectors not parallel to the thrust ramps. In particular, these backlimb panels

* Corresponding author. Tel.: +39 0654888049; fax: +39 0654888201.
E-mail address: tavani@uniroma3.it (S. Tavani).

0191-8141/$ - see front matter © 2005 Elsevier Ltd. All rights reserved.
doi:10.1016/j.jsg.2005.09.007

have a gentler dip than the underlying faults, as shown in the seismic section at the toe of the Cascadia accretionary prism (Fig. 1a). Generally, backlimb panels not parallel to thrust ramps and not produced by faulted detachment folding (e.g. Willis, 1893; Fischer et al., 1992) have been associated with fault-bend folding and related to either the accumulation of viscous material at the lower ramp inflection point (e.g. Jordan and Noack, 1992), or to an excess forelandward layer-parallel shear (Suppe et al., 2004). Backlimb panels not paralleling the ramp can also develop above lower inflection sectors in listric faults. Natural examples indicate, however, that backlimb panels not paralleling the ramp can also occur when none of the above mentioned conditions are satisfied. In the Cascadian accretionary prism, for example, the eastward convergence direction of the Juan de Fuca plate would likely induce a top-to-the-west excess layer parallel shear rather than an eastward shear, as required by the sheared fault-bend folding model of Suppe et al. (2004). Furthermore, in the more evolved anticline imaged in the seismic profile of Fig. 1a (right side), faulted layers located in the backlimb panel not paralleling the ramp are characterised by a rather constant footwall cutoff angle. This does not support the occurrence of a listric flat–ramp transition.

Another noticeable feature that is recognised in many anticlines at the toe of accretionary prisms is the evidence that thrust ramps in their early evolutionary stages may not be linked to either the basal or/and the upper décollement (e.g. Davis and Hyndman, 1989; Moore et al., 1990), as in the example from seismic line in the Nankai accretionary prism (Fig. 1b). Such a feature has also been recognised in thrust-related anticlines in fold-and-thrust belts (e.g. Williams and Chapman, 1983; Eisenstadt and De Paor, 1987; Ellis and Dunlap, 1988; Morley, 1994; McConnel et al., 1997) (Fig. 2a and b), as well as obtained in analogue models (e.g. Liu and Dixon, 1995; Storti et al., 1997) (Fig. 2c). Modelling of the stress field acting ahead of thrust sheets also indicates that the most suitable site for ramp nucleation can be located either in the upper part (Goff and Wiltschko, 1992) or in the central sector of the deforming multilayers (Storti et al., 1997).

We propose a new geometric and kinematic model, named double-edge fault-propagation folding, where the two main features illustrated above are implemented (Fig. 3). In this model, deformation occurs by flexural slip and bed thickness is preserved. The nucleation zone of thrust ramps can have a variable length and can be localised anywhere within the folded multilayers, regardless of the lower and upper décollement position. In the presented paper, only the case of ramp nucleated as a single segment/point is considered. In the more general case, fault ramps can also originate by the linkage of multiple fault segments (e.g. Eisenstadt and De Paor, 1987; Ellis and Dunlap, 1988; Cartwright et al., 1995; Childs et al., 1996). The resulting fold geometry is expected to be complex and its description is beyond the scope of this work. Double-edge fault-propagation folding also includes the possibility of varying the ramp slip versus propagation rate ratio (*S*/*P*; e.g. Williams and Chapman, 1983; McNaught and Mitra, 1993; Hardy and McClay, 1999) during fold growth, at both ramp tips. Total displacement is partitioned into slip along the ramp, folding, and layer-parallel shear. We provide the analytical formalisation of the model for both the circular hinge (e.g. Tavani et al., 2005) and the

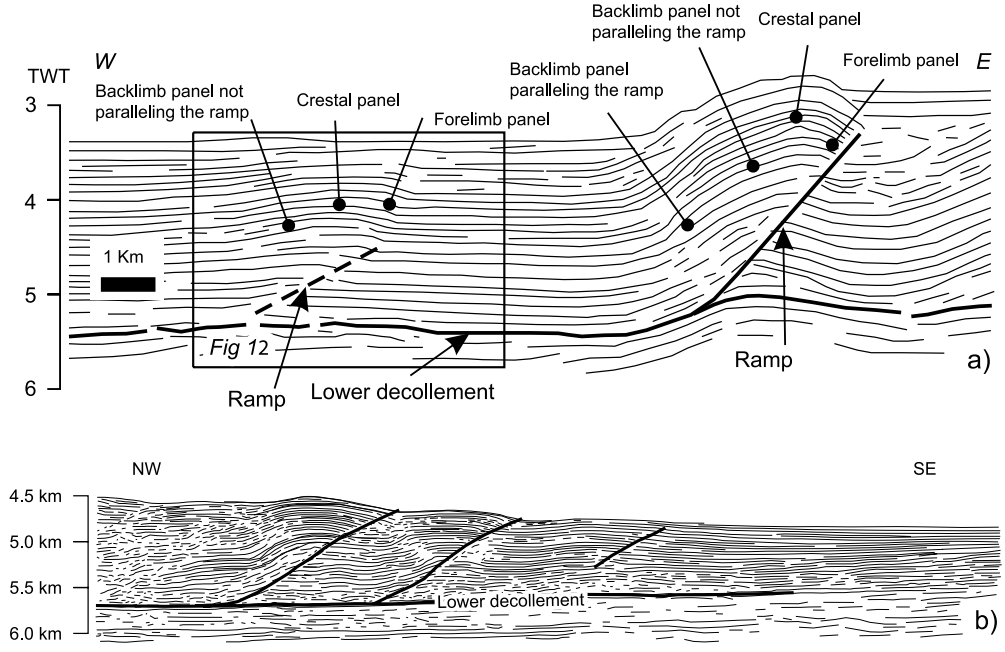

Fig. 1. Line-drawing of geoseismic cross-sections from modern accretionary prisms: (a) Cascadia accretionary prism (after Flueh et al., 1998); (b) Nankai accretionary prism (after Moore et al., 1990).

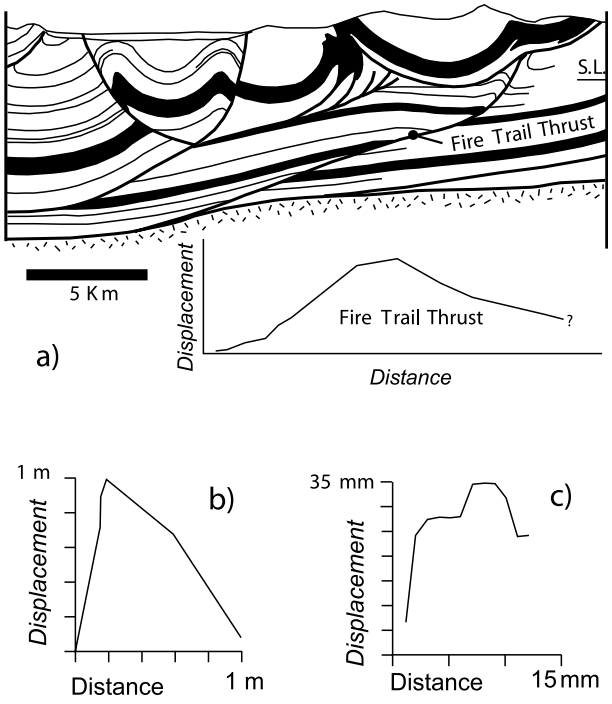

Fig. 2. Examples of displacement–distance diagrams associated with faults nucleated in the central sectors of the multilayers. The maximum displacement sites indicate the fault nucleation zones. (a) Fire Trail thrust in the Wyoming–Idaho thrust belt (USA) (after Ellis and Dunlap, 1988); (b) fault-related fold near Bergton (Virginia, USA) (after McConnel et al., 1997); (c) thrust-related anticlines in sandbox analogue models (after Storti et al., 1997).

kink-band geometrical solution (e.g. Suppe, 1983). Qualitative and quantitative comparisons with natural examples, and the discussion of the main features predicted by the model with respect to what has been described in the literature for natural structures, are used to illustrate the broad applicability of double-edge fault-propagation folding to contractional structures in thrust-and-fold belts and accretionary prisms.

2. Kinematic evolution of double-edge fault-propagation folding

The initial configuration of double-edge fault-propagation folding consists of a basal décollement accommodating layer-parallel contraction, and a thrust ramp nucleating somewhere within the multilayer (Fig. 3a). The ramp propagates by the upward and downward migration of the upper (Ut) and lower (Lt) tip, respectively. A ramp not connected to a layer-parallel décollement is here referred to as an immature ramp, a ramp linked to a basal décollement is referred to as a downward mature ramp, and a ramp connected with an upper flat is named an upward mature ramp. Hanging wall translation above a planar immature ramp symmetrically propagating at a constant up and down tip rate produces an anticlinal fold geometry consisting of

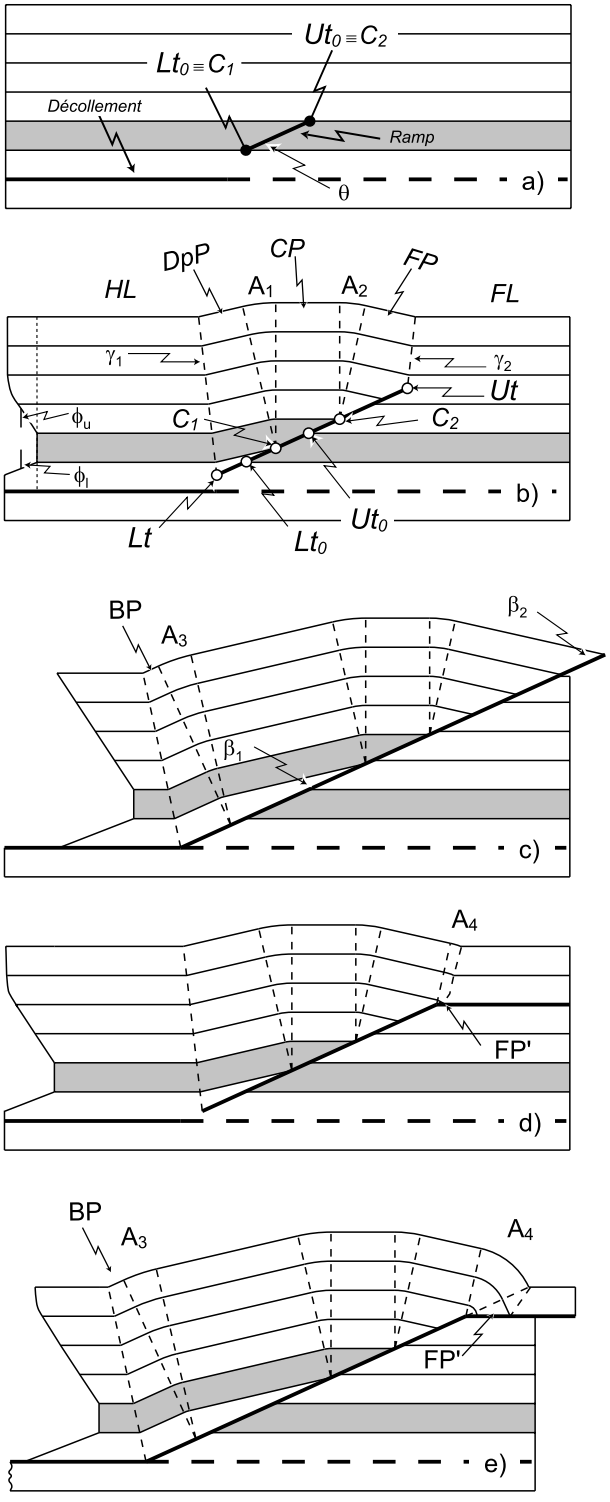

Fig. 3. Kinematic evolution of double-edge fault-propagation folding. (a) Pre-folding configuration; (b) ramp immature configuration; (c) downward mature ramp configuration; (d) upward mature ramp configuration; (e) transported double-edge fault-propagation folding. The light grey area indicates the layer faulted before hanging wall motion. Excess shear is positive when material is located to the left of the vertical line centred on the initially faulted layer; it is negative when it is located on the right. See text for details and labelling conventions.

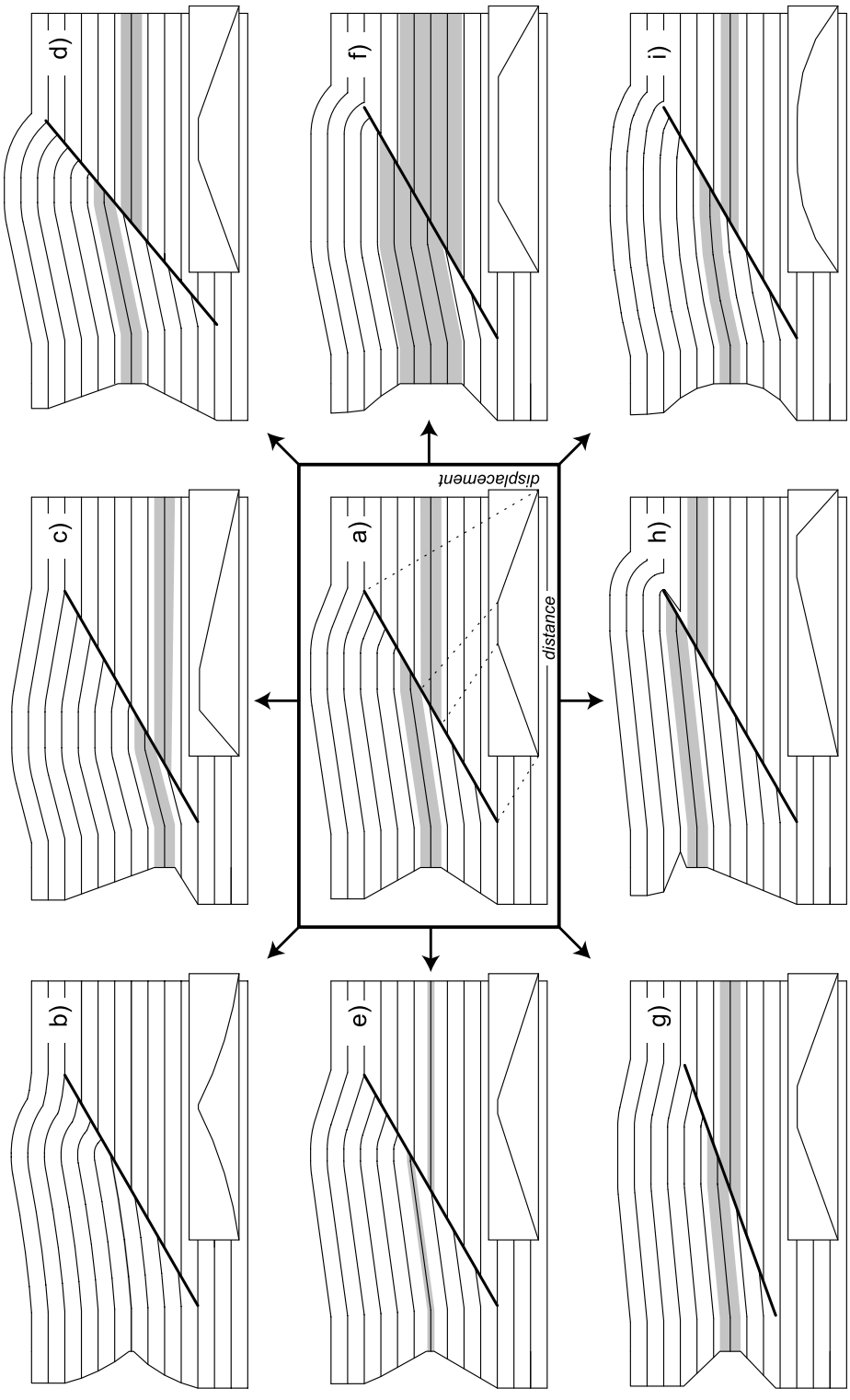

Fig. 4. Synoptic template showing the geometrical variability of double-edge fault-propagation folding induced by change in the ramp dip, ramp nucleation zone width and position, and *S*/*P* ratio of the fault tips. The inserts show the shapes of displacement–distance diagrams constructed along the ramps. The grey areas indicate the thickness of layers faulted before folding. See text for details.

five panels. These panels are referred to as hinterland (HL), downward propagation panel (DpP), crestal panel (CP), forelimb panel (FP), and foreland (FL), respectively (Fig. 3b). The DpP and CP panels are separated by the circular hinge sector A_2, pinned at the initial stratigraphical elevation of the lower ramp tip (C_1). Analogously, the FP and CP panels are separated by the circular hinge sector A_2, pinned at the initial stratigraphical elevation of the upper ramp tip (C_2). Two straight hinges (γ_1 and γ_2) are pinned at the lower and upper ramp tips and divide the HL from the DpP panels, and the FP from the FL panels, respectively. The upward and downward propagation of the upper and lower ramp tips causes the migration of the corresponding hinges γ_1 and γ_2 (active hinges; Suppe et al., 1992) and, consequently, the progressive widening of the DpP and FP panels by migration of material from the hinterland and the foreland, respectively (Fig. 3b). On the other hand, the circular hinge sectors A_1 and A_2 and the CP panel are passively translated along the ramp. The latter preserves its width during fold evolution. The lengths of the C_1–Lt_0 and C_2–Ut_0 segments correspond to the slip value along the ramp (S). The lengths of the Lt–Lt_0 and Ut–Ut_0 segments give the propagation value of the lower (P_l) and upper (P_u) ramp tips, respectively.

Excess layer-parallel shear occurs in the sectors of the multilayer stratigraphically underlying and overlaying A_1 and A_2, respectively. It increases during fold evolution and the final amount of layer-parallel shear for each layer depends on the residence time above the ramp (i.e. on both the S/P ratio and the ramp dip). This is because accumulation of excess shear in each layer terminates when it is cut by the fault tip. When the lower tip joins the basal décollement, the downward mature ramp stage starts and a new panel (BP) develops in the backlimb (Fig. 3c). The link between the BP and DpP panels is provided by the circular sector A_3, which is inactive, i.e. no material migrates across it (Suppe et al., 1992). On the other hand, if Ut joins a décollement layer while Lt is still migrating downward, the upward mature ramp stage starts and the FP panel is translated above the upper décollement. A new forelimb panel generates (FP′), divided from the FP panel by the active circular sector A_4 (Fig. 3d). Eventually, both the ramp tips joint a décollement layer, a staircase ramp trajectory forms, and the entire anticline is translated onto the foreland (Fig. 3e).

Fig. 4 illustrates the sensitivity of the fold shape to the S/P ratio, the ramp dip (θ), and the initial ramp length, i.e. the length of the segment C_1–C_2, for a given amount of contraction and final ramp length. Displacement–distance diagrams (e.g. Williams and Chapman, 1983) are used to visualise the influence of S/P and C_1–C_2. Model assumptions (i.e. flexural slip folding, bed thickness preservation, line-length preservation in the layers in between the ramp tips, and ramp nucleation at a single point/segment) imply that displacement–distance diagrams indicate fault propagation rates and directions. Furthermore, under these assumptions a univocal correspondence between the displacement–distance diagram and the fold shape occurs. The reference fold geometry (Fig. 4a) is characterised by a 30° dipping thrust ramp nucleated in its central sector with a discrete width C_1–C_2 that corresponds to the flat sector in the displacement–distance diagram. The ramp propagated upward and downward at the same rate and this is indicated by a straight and symmetric slope in the displacement–distance diagram. Changing the displacement–distance profile of the ramp to a symmetric, concave upward shape, i.e. increasing migration rate of the fault tips, produces a gentle upward concavity in both the backlimb and the forelimb sectors (Fig. 4b). A convex upward shape of the displacement–distance profile produces the significant smoothing of the fold profile, with a wider crestal zone. Both the forelimb and the backlimb sectors are characterised by a downward concave shape (Fig. 4i). Narrowing the initial ramp length C_1–C_2 produces a significant narrowing of the anticlinal crest (Fig. 4e), while the opposite occurs when the initial ramp length is widened. In the latter case, the narrow forelimb has a steeper dip (Fig. 4f). It is worth noting that a decrease of the slope in the displacement–distance diagram (Fig. 4e) corresponds to a decrease of the S/P ratio, while an increase of the slope (Fig. 4f) produces an increase of S/P. When the ramp dip decreases with respect to the reference one, both the backlimb dip and the forelimb dip decrease (Fig. 4 g). Conversely, a steeper ramp produces the steepening of both the fold limbs (Fig. 4d). Finally, an asymmetric displacement–distance profile implies a shallower or deeper location of the ramp nucleation zone and a variability of the S/P ratio along the ramp. In particular, a deeper nucleation zone causes a higher S/P ratio on the downward propagating ramp tip, and a lower S/P on the upward propagating one. This results in the shallowing and widening of the forelimb, and in the steepening and narrowing of the backlimb, while the crest width is preserved (Fig. 4c). A shallower ramp nucleation zone produces a high S/P ratio on the upward-migrating ramp tip, and a lower S/P on the downward-migrating one. This causes a strong fold asymmetry toward the foreland, dictated by a long and shallow-dipping backlimb, and by a narrow and steeply dipping forelimb (Fig. 4 h). It is worth noting that this kinematic configuration produces a footwall syncline.

To summarise, the initial length of the ramp nucleation zone imposes the width of the anticlinal crest, which is preserved during fold evolution. The S/P ratio of the ramp tips for a given ramp dip controls the limb dip. A decrease of S/P causes a shallowing of the backlimb and forelimb dip, whereas the opposite occurs when S/P increases. For a given S/P ratio, a decrease of the ramp dip produces a decrease of the limbs dip, and an increase of the ramp dip produces steeper fold limbs.

Two kinematic configurations among those illustrated in Fig. 4 deserve further detail.

(1) The progressive variation of the S/P ratio generates a number of constant-dip panels corresponding to the number

of straight segments with constant *S*/*P* ratio into which the distribution of *S*/*P* can be partitioned. Axial surfaces and/or circular sectors bounding adjacent panels are pinned at the stratigraphical elevations of the tips of these segments (Fig. 5). According to the guidelines described above, the progressive shallowing of the fold limbs away from the anticlinal crest can be produced by a decreasing of *S*/*P* ratio at the ramp tips and vice-versa (Fig. 5). Regardless of the fold limb convexity, it has to be emphasised that the segmentation of the fold limbs into several constantly dipping rock panels is produced by variation of the *S*/*P* ratio without any change of the ramp dip.

(2) High *S*/*P* ratios in the upper ramp tip cause development of a footwall syncline in the double-edge fault-propagation anticline (Fig. 6). The fold is articulated into six panels because the footwall syncline panel (SP)

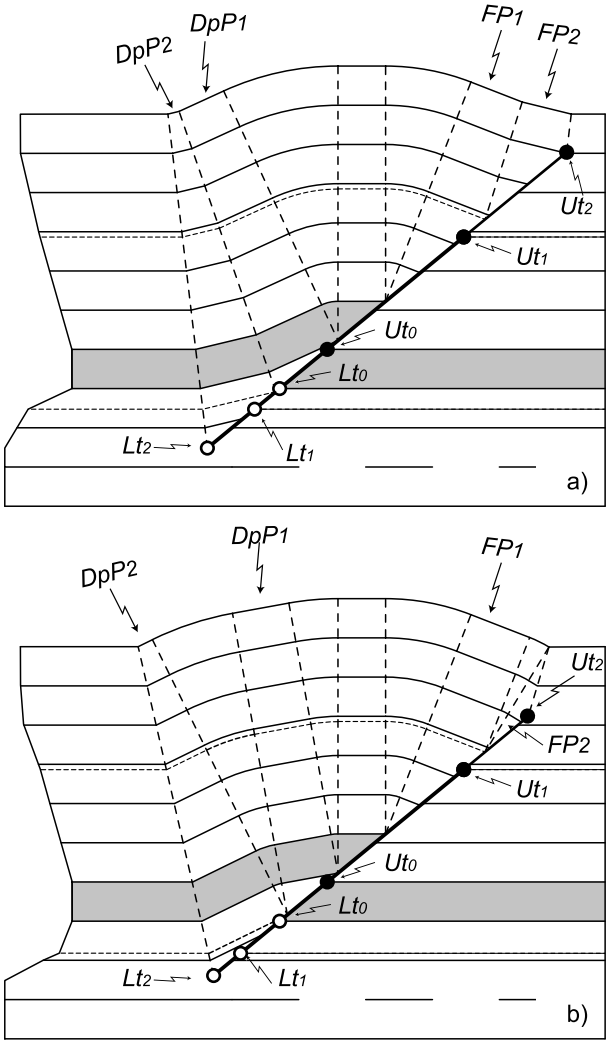

Fig. 5. Variability of fold shapes produced by double-edge fault-propagation folding at variable *S*/*P* ratios. (a) The *S*/*P* ratio decreases at both the fault tips during their propagation, causing the progressive shallowing of the limbs dip. (b) The *S*/*P* ratio increases at both the fault tips during their propagation, causing the progressive steepening of fold limbs. See text for details.

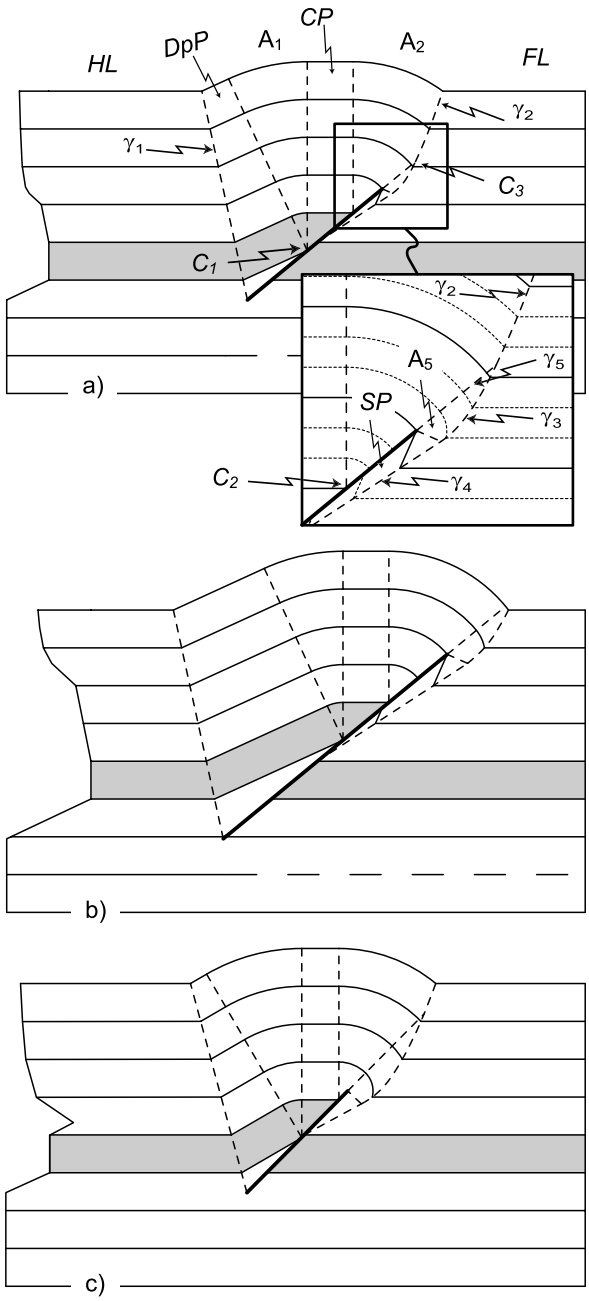

Fig. 6. Kinematic evolution of double-edge fault-propagation folding when a footwall syncline develops. (a) Internal architecture of the anticline; (b) fold geometry when both the ramp tips propagate upward and downward, respectively; (c) fold geometry with footwall syncline associated with a steeper ramp. Note that in this case a negative excess layer-parallel shear occurs.

adds to the standard configuration described in Fig. 3. The DpP and CP panels preserve their architecture, the FP panel disappears, and the ramp defines the external boundary of the circular hinge sector A_2. A new circular sector (A_5) is pinned at the upper ramp tip and is divided from the foreland panel (FL) by the active axial surface γ_3. The SP panel is separated from HL by the inactive axial surface γ_4. The axial surfaces γ_5 is located along the upward prosecution of

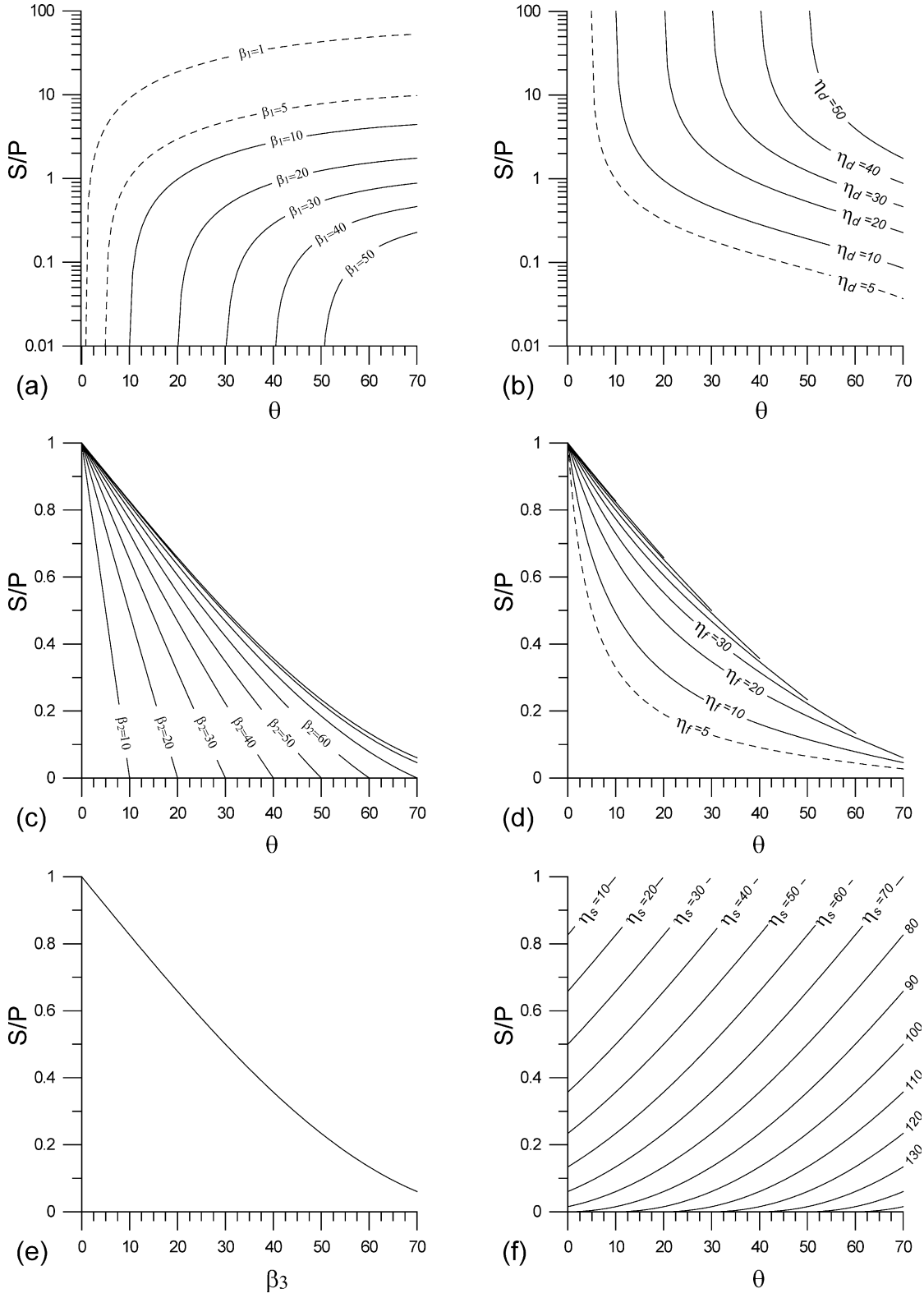

Fig. 7. Graphical solutions for the parameters describing double-edge fault-propagation folding. The graph (a) relates S/P_l, θ and β_1. Graph (b) relates S/P_l, θ and the dip of the DpP panel (η_d). Graph (c) relates S/P_u, θ and β_2 (solution without footwall syncline). Graph (d) relates S/P_l, θ and the dip of the FP panel (η_d). Graph (e) relates S/P_u, θ and β_3 (solution with footwall syncline). Graph (f) relates S/P_l, θ and the dip of the SP panel (η_s is positive when hinterlandward dipping).

the ramp and joins γ_3 at the triple point C_3. Fold growth occurs by progressive migration of material from the foreland into the circular hinge sectors A_2 and A_5. The upward migration of the upper ramp tip implies the upward migration of the circular sector A_5 and, consequently, the widening of the SP panel.

Progressive fold growth imposes a positive excess layer-parallel shear in the layers stratigraphically overlaying point C_3, and a negative excess layer-parallel shear in the underlying layers. The upward migration of the upper ramp tip and, consequently, of point C_3, imposes the superimposition of negative excess shear in those layers previously affected by positive shear. The resulting shear profile depends on the sum of the two components and can be either positive or negative (Fig. 6b and c).

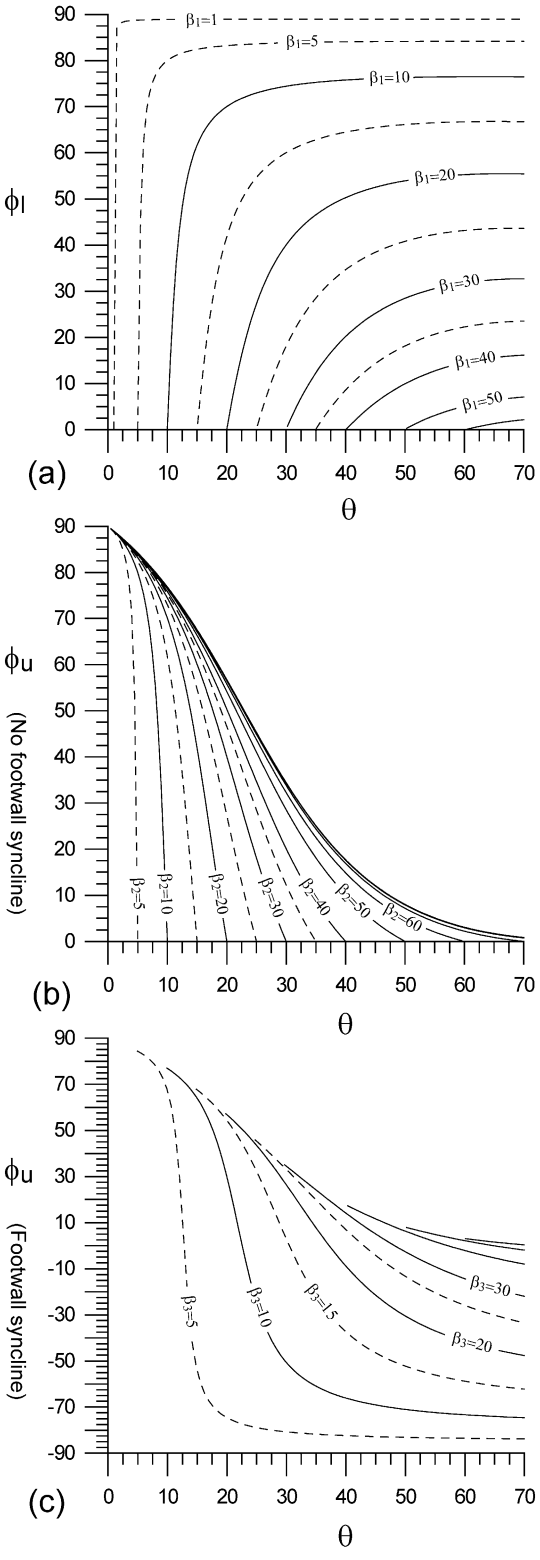

Fig. 8. Graphs relating the excess layer parallel shear, the ramp dip, and the cutoff angles associated with double-edge fault-propagation folding.

3. Analytical solutions of double-edge fault-propagation folding

The quantitative description of double-edge fault-propagation folding includes the formalisation of geometrical relationships among angular and linear parameters, and in particular between the cutoff angles of the DpP, FP and SP panels, the *S*/*P* ratio associated with the lower and upper ramp tips, and the ramp dip (θ). Equations describing angular parameters are listed below and their graphical solutions are illustrated in Figs. 7 and 8. The complete derivation of the equations is provided in the Appendix.

The S/P_l ratio associated with the lower ramp tip relates to the ramp dip (θ) and to the cutoff angle of the DpP panel (β_1) through the following equation:

$$\frac{S}{P_l} = \frac{\sin(\theta)}{\sin(\beta_1)} - 1 \tag{1}$$

with S being the slip along the ramp (C_1–Lt_0 segment in Fig. 3) and P_l the associated lower ramp tip propagation (Lt–Lt_0 segment in Fig. 3). The excess layer-parallel shear angle associated with the lower ramp tip propagation (ϕ_l) relates to both θ and β_1 through the following equation:

$$\tan(\phi_l) = \frac{[\sin(\theta) - \sin(\beta_1)]^2}{\sin(\theta - \beta_1)\sin(\beta_1)\sin(\theta)} \tag{2}$$

Analogously, the S/P_u ratio associated with the upper ramp tip relates to the ramp dip (θ) and to the cutoff angle of the FP panel (β_2) through the following equation:

$$\frac{S}{P_u} = 1 - \frac{\sin(\theta)}{\sin(\beta_2)} \tag{3}$$

with S being the slip along the ramp and P_u the associated upper ramp tip propagation (Ut–Ut_0 segment in Fig. 3). Eq. (3) can also be written as:

$$\beta_2 = \arcsin(Q) \tag{4}$$

with

$$Q = \left[\frac{\sin(\theta)}{1 - \frac{S}{P_u}}\right] \tag{5}$$

The angular value of the excess layer-parallel shear associated with the propagation of upper ramp tip (ϕ_u) relates to both θ and β_3 through the following equation:

$$\tan(\phi_u) = \cot(\theta) - \cot(\beta_2) - (\theta - \beta_2) \quad (6)$$

The condition $Q \leq 1$ imposes that the following equation must be verified:

$$\frac{S}{P_u} \leq 1 - \sin(\theta) \quad (7)$$

When $\frac{S}{P_u} = 1 - \sin(\theta)$, β_2 is 90° and the FP panel disappears.

When the values of the S/P_u ratio do not satisfy Eq. (7), the kinematic solution with footwall syncline develops. In this case, the S/P_u ratio associated with the propagation of the upper ramp tip relates to the SP panel cutoff angle (β_3) through the following equation:

$$\frac{S}{P_u} = 1 - \sin(\beta_3) \quad (8)$$

This equation does not depend on the ramp dip and can be written as:

$$\beta_3 = \arcsin\left[1 - \frac{S}{P_u}\right] \quad (9)$$

The angular value of the excess layer-parallel shear associated with the propagation of the upper ramp tip (ϕ_u) relates to both θ and β_3 through the following equation:

$$\tan(\phi_u) = \cot(\theta) - \left(\frac{\pi}{2} - \theta\right) - \left\{\frac{[\sin(\theta) - \sin(\beta_3)]^2}{\sin(\theta)\sin(\beta_3)\sin(\theta + \beta_3)}\right\} \quad (10)$$

The geometrical construction of double-edge fault-propagation anticlines with rounded hinge zones starts from the ramp dip θ, which is obtained by linking the curvature centres of the circular hinge sectors (Figs. 3, 5 and 6) (e.g. Tavani et al., 2005). Entering θ and either the DpP panel cutoff angle (β_1) or the DpP panel dip angle (η_d) in graphs (a) or (b) of Fig. 7 allows to obtain S/P_l. The intersection between the fault trace and the axial surface dividing the HL and DpP panels provides the position of the lower ramp tip (Lt) (Fig. 3). Analogously, entering θ and the FP panel cutoff angle (β_2) or the FP panel dip angle (η_f) in graphs (c) or (d) of Fig. 7 provides S/P_u. The intersection between the fault trace and the axial surface dividing the FP and FL panels permits the position of the upper ramp tip to be obtained (Fig. 3). The possibility of obtaining the position of the ramp tips in two ways provides a better constraint on the ramp geometry of natural structures. When a footwall syncline develops, the S/P_u ratio is obtained by entering the SP synclinal panel cutoff angle (β_3) or the SP panel dip angle (η_s) in graphs (e) or (f). The amount of excess layer-parallel shear associated with the fold growth is obtained by entering the ramp dip and the cutoff angles in graphs (a) and (b) or (c) of Fig. 8.

Eqs. (1), (3) and (8) allow one to construct the internal architecture of double-edge fault-propagation anticlines by using both circular hinge sectors (e.g. Julivert and Arboleya, 1984; Tavani et al., 2005) and kink-bands (e.g. Ramsay, 1974; Suppe, 1983). The kink-style geometry for the same angular and linear parameters is obtained by replacing circular hinge sectors with straight axial surfaces (Fig. 9). In the kink-style configuration, Eq. (3) permits two solutions: a first one with $\beta_3 < 90°$ (Fig. 9a) and a second one with $\beta_3 > 90°$ (Fig. 9b). Analogous to fault-bend folding (Suppe, 1983), these solutions are named Mode I ($\beta_3 < 90°$) and Mode II ($\beta_3 > 90°$), respectively. Different internal architectures between rounded and kink-style configurations imply that values of ϕ_u for the kink-style configuration differs from that of Eqs. (6) and (10), in particular, Eq. (6) is

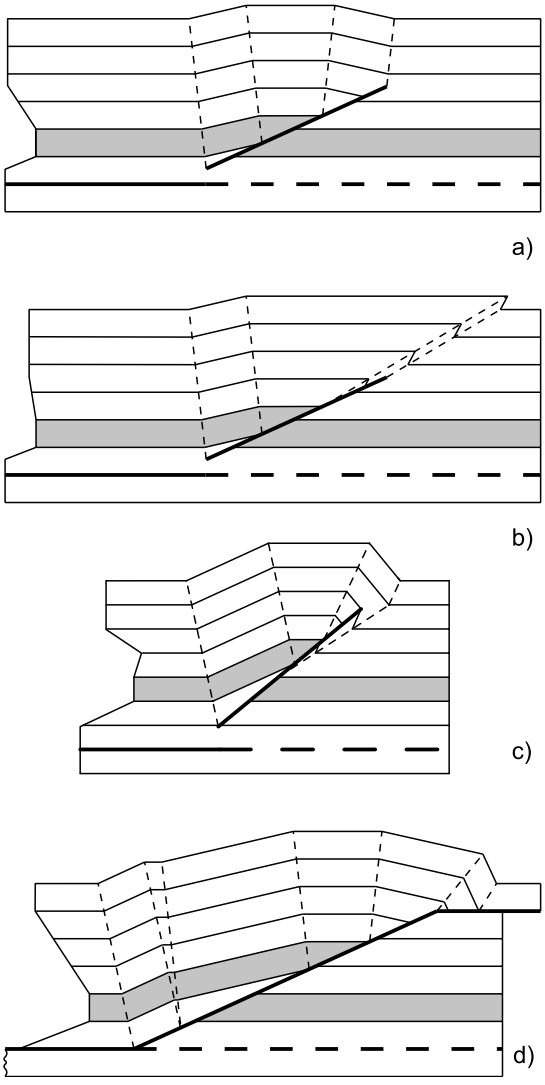

Fig. 9. Kink-style double-edge fault-propagation folding: (a) geometry produced by Mode I solution; (b) geometry produced by the Mode II solution; (c) geometrical configuration with footwall syncline; (d) transported double-edge fault-propagation folding with kink-style geometry.

replaced by:

$$\tan(\phi_u) = \cot(\theta) - \cot(\beta_2) - 2\tan\left(\frac{\theta-\beta_2}{2}\right) \quad (11)$$

Eq. (10) is replaced by:

$$\tan(\phi_u) = \cot(\theta) - 2\tan\left(\frac{\pi}{4}-\frac{\theta}{2}\right) - \left\{\frac{[\sin(\theta)-\sin(\beta_3)]^2}{\sin(\theta)\sin(\beta_3)\sin(\theta+\beta_3)}\right\} \quad (12)$$

The main difference between the two hinge styles concerns the transition between the DpP and BP panels characterising the downward mature ramp stage. In the kink-style configuration, this transition is in fact provided by a small and flat-lying triangular panel (Fig. 9d).

When the circular hinge geometry is adopted and the *S*/*P* ratio of both the lower and upper ramp tips changes during faulting, Eqs. (1), (3) and (8) provide the cutoff values of the last developed panel. During the propagation of the upper ramp tip, the most external panel is the last developed one and, consequently, it does not cause any modification to the cutoff angles of the previously developed panels. Conversely, the youngest panel developed ahead of the lower ramp tip is the most internal one. If its dip is greater than that of the adjacent panel, line-length preservation in the layers stratigraphically higher than the lower ramp tip implies modification of the cutoff values of all the previously developed panels. Such instantaneous modifications of the hanging wall cutoff values are unlikely in nature. Alternatively, cutoff values can be preserved by assuming a slight amount of layer-parallel shortening in the layers stratigraphically higher than the lower ramp tip. This amount depends on the apical angle of the circular hinge sector dividing the younger panel from the adjacent one. It is negligible for small apical angles, reaching 2% when the latter is 30°, and exceeds 5% of the circular hinge sector length only when the apical angle is greater than 45°. A similar problem occurs when the ramp links to the basal décollement. The adoption of a circular hinge sector dividing the BP and DpP panels (Fig. 3c and d) implies a slight modification in the cutoff values of the DpP, CP and FP panels to preserve their line-length. The amount of line-length reduction required to preserve the cutoff angles is lower than 0.4% of the DpP panel length when the ramp angle is 30°. Such a reduction is about 2.5% of the DpP panel length when the ramp angle is 40° and can increases up to 7.1% for ramp angles exceeding 50°.

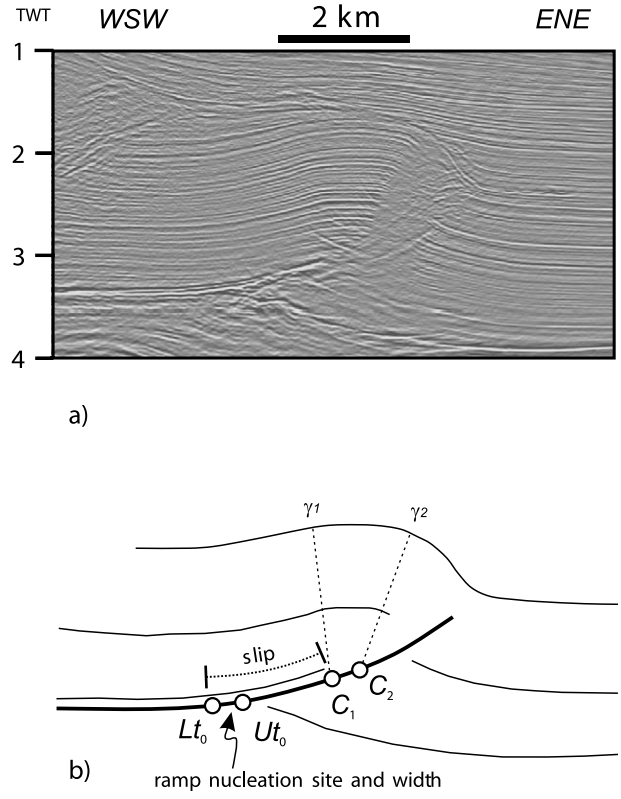

Fig. 10. Qualitative interpretation of the Basil anticline, the Adriatic foredeep, Italy, as a double-edge fault-propagation fold developed above a ramp emanated from the basal décollement. (a) Seismic cross-section (after Storti et al., 2004). (b) Schematic line-drawing showing the main kinematic features that can be obtained by the TWT image. See text for details.

4. Application to natural examples

Comparison between the main geometric features of faults and folds in Fig. 1, and model predictions in Fig. 3, indicates that the former can be all successfully reproduced by double-edge fault-propagation folding. Natural examples also include fault–fold geometries that resemble the two end member solutions of the double-edge fault-propagation fold kinematics, i.e. ramp nucleation from the lower and upper décollement, respectively. The first solution can be proposed for the Basil anticline, a fault-propagation fold in the Adriatic foredeep of the Northern Apennines, Italy (Storti et al., 2004). Despite the seismic profile acquired across this anticline, it is not depth-converted and, consequently, it does not allow precise and quantitative modelling; qualitative comparison reveals diagnostic features supporting double-edge fault-propagation folding. The anticline is characterised by a long and shallow-dipping backlimb, and by a narrow and steeply dipping forelimb (Fig. 10). The apparent lack of layer thickening in the anticlinal core does not support faulted detachment folding (e.g. Willis, 1893; Fischer et al., 1992; Mitra, 2003). Fold limbs are separated by a flat-lying crestal sector, which can be traced down to the fault trace. This feature is not predicted by 'classical' fault-propagation folding models (e.g. Mitra, 1990; Suppe and Medwedeff, 1990), which require the progressive downward narrowing of the crestal panel and its disappearance in the lower part of the folded multilayer. In double-edge fault-propagation folding, tracing the boundaries of the crestal sector down to the fault trace allows one to locate points C_1 and C_2 that, in turn,

provide the initial length of the ramp nucleation zone (Fig. 10b). Restoration of these points to their pre-folding stratigraphic elevations provides the position of the lower (Lt_0) and upper (Ut_0) ramp tip, respectively. Depending on the adopted fold style (i.e. kink-band versus circular hinge sectors), the location of points C_1 and C_2 and, consequently, the width of the C_1–C_2 segment, can vary within an approximation range that is intrinsic in the geometrical modelling. Despite such an uncertainty, the position of the point Lt_0 remains very close to the lower décollement and this suggests that the ramp nucleated at the basal décollement, which is consistent with the absence of the DpP panel.

Fault–fold geometries resembling those associated with a double-edge fault-propagation fold nucleated from the upper décollement can be proposed for the anticline described in the Maracaibo Basin by Apotria and Wilkerson (2002). According to the authors, in this structure the ramp sector of the thrust nucleated from the upper décollement and then propagated downward, eventually joining the basal décollement. The line-drawing in Fig. 11a shows the fault–fold architecture in the mature stage, which is characterised by a backlimb panel not parallel to the ramp. This panel is linked to the basal décollement by a ramp-parallel backlimb sector. Progressive unfolding of the anticline allows inferring the evolutionary pathway of the structure and the pre-folding configuration, which is characterised by a wide nucleation zone of the thrust ramp (Fig. 11b).

A quantitative application of double-edge fault-propagation folding can be tested in the embryonic anticline imaged in the seismic line of Fig. 1a. In the depth converted geoseismic cross-section, both the anticlinal limbs and a wide thrust ramp zone are well imaged (Fig. 12). A flat lying attitude characterises strata below the fault. The average dip of the DpP panel is about 7.7° and the dip of the FP panel is 9.1°. The dip of the ramp is 30.7°, and the regional dip in the

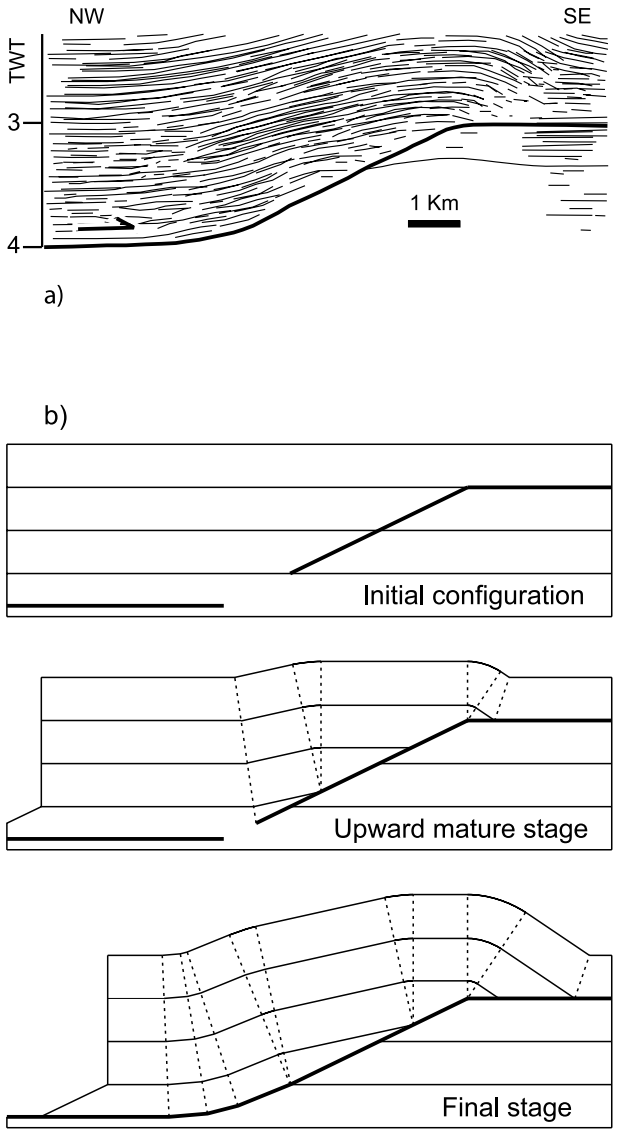

Fig. 11. Example of a thrust-related fold in the Maracaibo Basin, Venezuela, that can be interpreted as a double-edge fault-propagation anticline developed above a ramp emanated from the upper décollement. (a) Line-drawing of the original seismic cross-section (in Apotria and Wilkerson, 2002). (b) Cartoon showing the progressive evolution from the pre-folding stage up to the present stage.

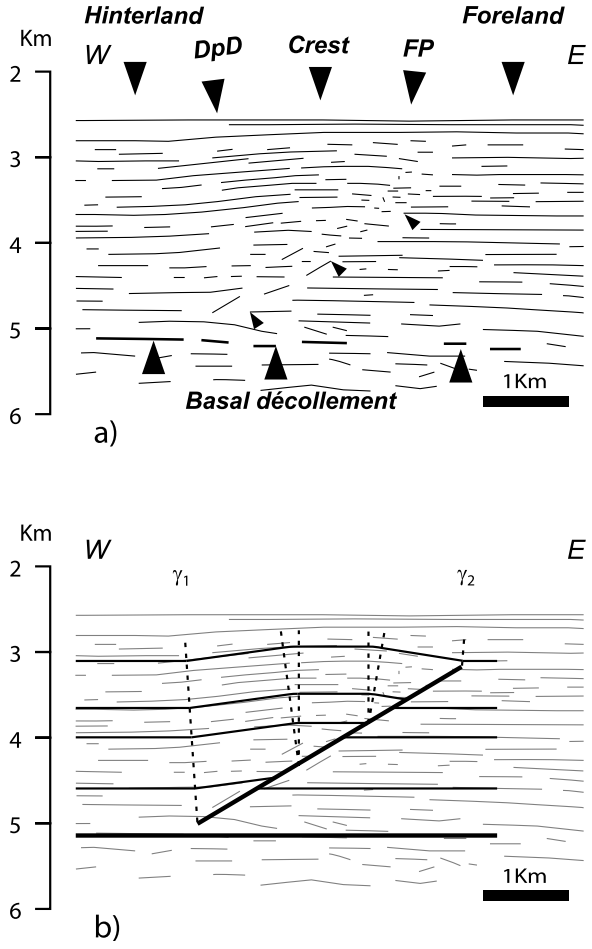

Fig. 12. Quantitative modelling of the embryonic structure at the toe of the Cascadia accretionary prism (after Flueh et al., 1998) as a double-edge fault-propagation anticline. See text for details.

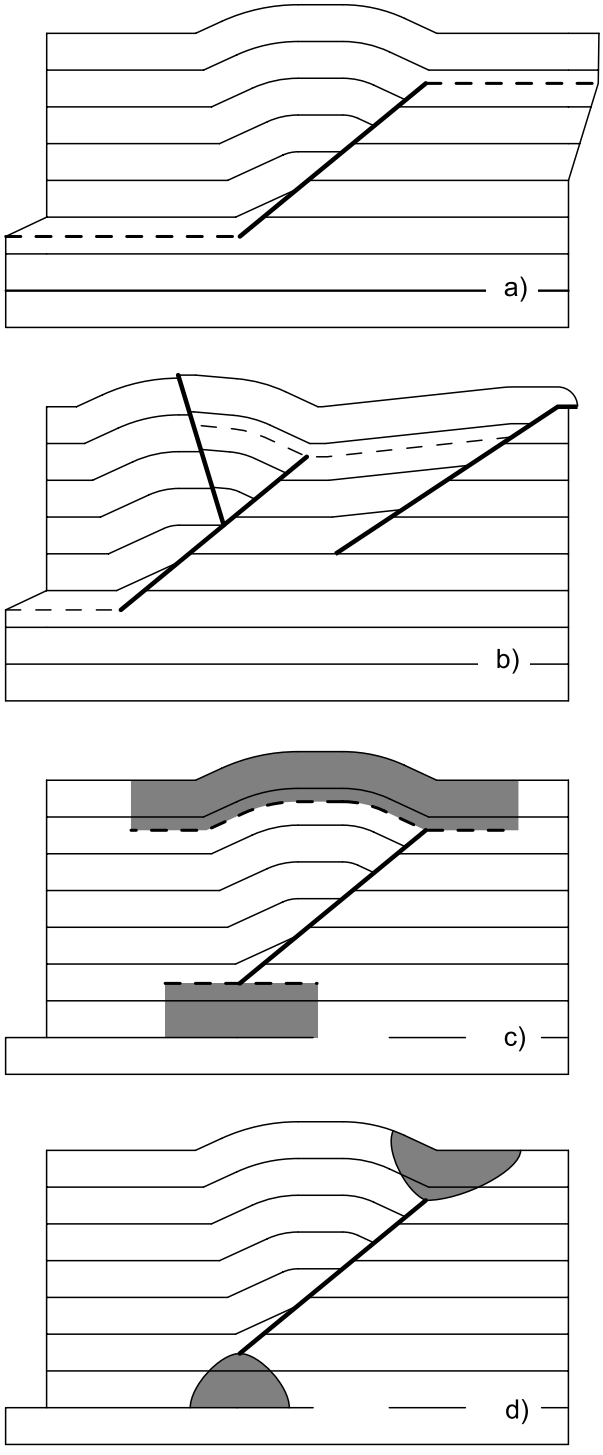

Fig. 13. Different possible mechanisms accomplishing excess layer parallel shear associated with double-edge fault-propagation folding. (a) Development of transient décollements at ramp tips to transfer excess shear outward of the growing anticline; (b) shear accommodated by discrete thrusting within and outward of the growing anticline; (c) shear accommodated by layer-parallel shortening distributed across the fold; (d) shear accommodated by layer-parallel shortening localised near the fault tips. See text for details.

folded area is about 0°. To construct the fold geometry, we start by locating the lower ramp tip at the intersection between the axial surface γ_1, dividing the DpP and the HL panels, and the trace of the ramp (Fig. 12b). The intersection between the axial surface γ_2, dividing the FP and FL panels, and the ramp trace, gives the position of the upper ramp tip (Fig. 12b). The anticline is then completed by tracing the circular hinge sectors A_1 and A_2 that are pinned to the ramp. The smoothed fold geometry in fact favours the adoption of rounded hinges instead of angular ones. Using kink-style folding, however, does not substantially change the final fold architecture. Entering the obtained cutoff values of the rock panels DpP and FP, and the ramp dip into graphs (a) and (b) of Fig. 7 provides the *S*/*P* ratio of the lower and upper ramp tips, respectively. The *S*/*P* value for the lower tip is 0.31 while for the upper tip it is 0.20. The predicted amount of excess layer-parallel shear can be obtained by graphs of Fig. 8. Accordingly, ϕ_l is $+28.4°$ and ϕ_u is $+18.0°$, respectively.

The lack of evidence of disharmonic thickening in the fold core and the flat lying attitude of the footwall strata do not support the interpretation of this structure as a faulted décollement anticline. Interpretation of the structure as an eastward sheared fault-bend anticline is discarded according to what is discussed in Section 1.

5. Discussion

5.1. Excess layer-parallel shear accommodation

In many cases, excess-layer parallel shear in double-edge fault-propagation folding can be regarded as a geometrical artefact, which is progressively compensated by deformation during fold growth (e.g. Tavani et al., 2005). This bed-thickness-preserving, folding-related deformation can occur at either constant (e.g. Mitra, 1990) or variable (e.g. Geiser, 1988) line-length. Application of the first solution to our model implies that two transient layer-parallel décollements are simultaneously activated at ramp tips during every increment of fault propagation, and then they are rapidly abandoned at the next increment of outward migration of the ramp tips (Fig. 13a). In most cases, excess layer-parallel shear can be accommodated by second-order folding and thrusting either outside (e.g. Mitra, 1990) or within the anticline (e.g. Mitra, 2002). Hybrid solutions where part of the excess shear is transferred to the foreland and/or to the hinterland likely occur (Fig. 13b). When deformation does not preserve line-length, the excess layer-parallel shear has to be compensated by layer-parallel shortening at constant bed thickness (e.g. pressure solution cleavage) (Fig. 13c). The width of the cross-sectional area affected by layer-parallel shortening depends on the factors that contribute to determine the length of the transient décollements developing at the migrating ramp tips, i.e. the efficiency of the layer-parallel shear. These factors include

the rock type and initial porosity, fluid flow, strain rate and temperature, which control the effectiveness of layer dissolution (e.g. Rutter, 1983), and the interlayer rheology, which controls the frictional coupling among adjacent beds (e.g. Donath and Parker, 1964). A progressively widening deformation area away from the migrating ramp tip (Fig. 13d) is expected to maximise the efficiency of the process. For the propagation of the upper ramp tip, such a deformation zone shape resembles that predicted by the trishear kinematic model of fault-propagation folding (e.g. Erslev, 1991; Zehnder and Allmendinger, 2002). A geometrical similarity, however, does not necessary mean a kinematic similarity because bed thickness is not preserved by the latter kinematic model.

The upward increase of the bed length along which layer-parallel shortening generated by the upper ramp tip propagation is accommodated, generates a layer-parallel shear with a sense of slip of top-to-the-crest in the forelimb and top-to-the-foreland in the foreland sector. Such a shear distribution is recognised in natural fault-propagation anticlines (e.g. Fisher and Anastasio, 1994; Erslev and Mayborn, 1997). The widespread occurrence of layer-parallel shortening in accretionary prisms and thrust-and-fold belts (e.g. Alvarez et al., 1978; Marshak and Engelder, 1985; Mitra and Yonkee, 1985; Casas and Muñoz, 1987; Geiser, 1988; Srivastava and Engelder, 1990; Averbuch et al., 1992; Morgan and Karig, 1995; Sans et al; 2003; among others), supports the efficacy of this mechanism to accommodate the excess layer-parallel shear associated with double-edge fault-propagation folding.

5.2. Mechanical stratigraphy and deformation environment

The interdependence of fold shape, ramp nucleation site and width, and ramp slip versus propagation rate that characterises double-edge fault-propagation folding, allows one to indirectly assess the role of the mechanical stratigraphy (e.g. Corbett et al., 1987; Fischer and Jackson, 1999; Chester, 2003) and environmental conditions of deformation (e.g. Jamison, 1992) into geometric–kinematic modelling of fault–fold interaction. It has been recognised that the initial length of the ramp and its position are influenced by both lithology (e.g. Eisenstadt and De Paor, 1987; Childs et al., 1996) and stress conditions during deformation; regardless of the basal décollement position (e.g. Goff and Wiltschko, 1992; Storti et al., 1997). Analogously, ramp propagation rate is influenced by the mechanical properties of the faulted rock multilayer and, consequently, it can vary through time (e.g. Muroaka and Kamata, 1983; Walsh and Watterson, 1988). The implementation of these parameters (i.e. *S*/*P* ratio, ramp nucleation site and width) in double-edge fault-propagation folding allows us to take into account their variability during fold growth. It has to be emphasised that mechanical stratigraphy and fold growth mutually interact in a feedback mechanism. In fact, deformation induced ahead of ramp tips by fold growth changes the mechanical properties of the rocks. This in turn influences both the geometry of the newly forming ramp segments and their *S*/*P* ratios, thus modifying the new fold shape and, consequently, the deformation pattern associated with it. When considered in four dimensions, this process implies an along strike variability of the fold architecture, caused by the diachronous lateral propagation of the fault–fold pair (e.g. Medwedeff, 1992; Mueller and Suppe, 1997).

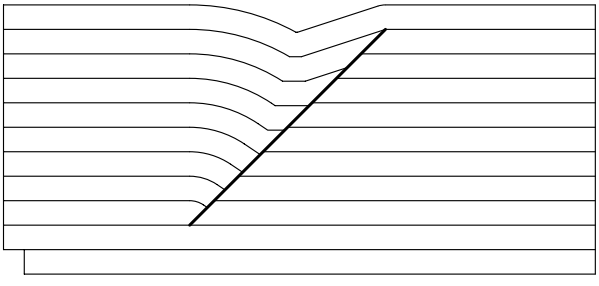

Fig. 14. Example of hanging wall geometry produced by extensional double-edge fault-propagation folding.

5.3. Insights for extensional double-edge fault-propagation folding

Implementation of parameters, like the position of the ramp nucleation zone and its initial length, and the slip versus propagation rate of the ram tips, makes double-edge fault-propagation folding a kinematic mechanism suitable to be implemented for extensional tectonic environments. Preliminary results of the application of double-edge fault-propagation folding to extensional deformations (Fig. 14) show the possibility of successfully modelling diagnostic features like rollover anticlines (e.g. Hamblin, 1965; Xiao and Suppe, 1992) or hanging wall synclines (e.g. Gawthorpe et al., 1997), and their coexistence along the same fault ramp.

6. Conclusion

We developed a new geometric and kinematic model of fault-propagation folding, here referred to as double-edge fault-propagation folding, which permits simulation of folding associated with thrust ramps nucleated within the rock multilayer and characterised by variable initial length and variable *S*/*P* ratios. Coeval upward and downward propagation of the thrust ramp produces folding in the hanging wall predating its forelandward translation above the thrust ramp. A diagnostic feature of this stage is the development of a backlimb panel, related to the downward ramp propagation, which has a dip toward the hinterland that is systematically lower than the ramp dip.

For a given ramp dip, the dip of the backlimb and forelimb panels depends on the *S*/*P* ratio at the ramp tips. This means that (1) different fold shapes are produced by

different *S*/*P* ratios and (2) incremental variations of *S*/*P* produces corresponding progressive variations of the fold shape, i.e. the univocal relationship between fault and fold segmentation is released. When a critical *S*/*P* value is exceeded, a new geometrical configuration develops, characterised by the presence of a footwall syncline. The dependence of the fold shape and the fault behaviour (i.e. *S*/*P* and nucleation site and width) on the mechanical stratigraphy of the deforming rock multilayer, provides the way to indirectly implement the influence of this parameter in geometrical modelling.

The evolution of double-edge fault-propagation folding produces an excess layer-parallel shear in the growing anticlines. In many cases, such a shear can be regarded as a geometrical artefact that is compensated at constant bed thickness by second order folding and/or layer-parallel shortening, either distributed along the entire cross-sectional area of the fold or concentrated in deformation zones ahead of the ramp tips. In the latter solution, a triangularly shaped deformation zone is expected to originate at the ramp tips.

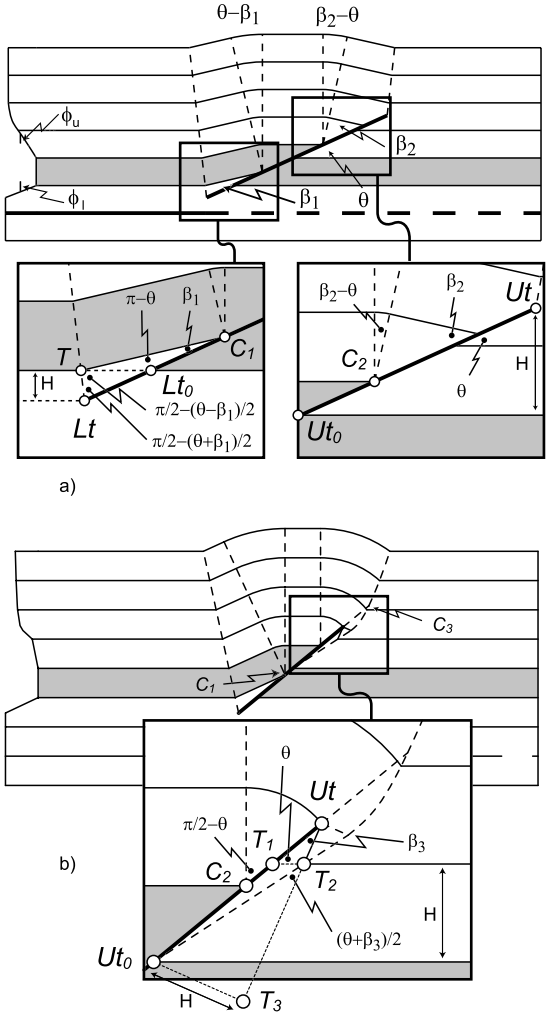

Fig. 15. Geometrical constructions for Eqs. (1)–(11).

The occurrence in many thrust related anticlines of diagnostic features predicted by double-edge fault-propagation folding supports the broad applicability of this kinematic model to natural structures. The basic kinematic assumption of fault and fold behaviours in compressional environments can be successfully implemented in extensional fault-related structures.

Acknowledgements

We thank D. Frizon de Lamotte and A. Nicol for their comments, which were very helpful in improving the paper. Funding for this research was provided by the Italian MIUR (Ministero dell'Istruzione, dell'Università e della Ricerca), grants awarded to F. Salvini. Software for simulating the geometry of double-edge fault-propagation folding is available for free download at http://host.uniroma3.it/progetti/fralab/.

Appendix

Eq. (1) (see Fig. 15a).

The length of the C_1–Lt_0 segment gives the slip along the ramp (S). The propagation of the lower ramp tip (P_1) is given by the Lt–Lt_0 segment length. S relates to the length of the T–Lt_0 segment through the following equation:

$$T - \mathrm{Lt}_0 = \frac{S}{\sin(\theta - \beta_1)} \sin(\beta_1) \tag{A1}$$

Analogously, P relates to the length of the T–Lt_0 segment through the following equation:

$$T - \mathrm{Lt}_0 = \frac{P_1}{\sin\left(\frac{\pi}{2} - \frac{\theta - \beta_1}{2}\right)} \sin\left(\frac{\pi}{2} - \frac{\theta + \beta_1}{2}\right) \tag{A2}$$

By comparing Eqs. (A1) and (A2), simplifying and rearranging, we obtain:

$$\frac{S}{P_1} = \frac{\cos\left(\frac{\theta+\beta_1}{2}\right)}{\cos\left(\frac{\theta-\beta_1}{2}\right)} \frac{\sin(\theta - \beta_1)}{\sin(\beta_1)} \tag{A3}$$

Eq. (A3) can be written also as:

$$\frac{S}{P_1} = \frac{2\cos\left(\frac{\theta+\beta_1}{2}\right)\sin\left(\frac{\theta-\beta_1}{2}\right)}{\sin(\beta_1)} \tag{A4}$$

by using the prostapheresis formula and simplifying:

$$\frac{S}{P_1} = \frac{\sin(\theta)}{\sin(\beta_1)} - 1 \tag{1}$$

Eq. (2) (see Fig. 15a).

The amount of excess layer-parallel shear at the stratigraphic elevation of Lt corresponds to the slip along the basal décollement. This is given by the difference given between T–C_1 and T–Lt_0 segments length. Consequently the following equation must be verified:

$$H\tan(\phi_1) = (T - C_1) - (T - \mathrm{Lt}_0) \quad \text{(A5)}$$

The length of segment T–C_1 is provided by the following equation:

$$T - C_1 = \frac{S}{\sin(\theta - \beta_1)}\sin(\pi - \theta) \quad \text{(A6)}$$

H relates to P_1 through the following equation:

$$H = P_1\sin(\theta) \quad \text{(A7)}$$

By substituting Eqs. (A2), (A6) and (A7) into Eq. (A5), and simplifying we obtain:

$$\tan(\phi_1) = \frac{S}{P_1\sin(\theta - \beta_1)} - \frac{\cos\left(\frac{\theta+\beta_1}{2}\right)}{\cos\left(\frac{\theta-\beta_1}{2}\right)\sin(\theta)} \quad \text{(A8)}$$

By substituting Eqs. (A3) and (1) into Eq. (A8) we obtain:

$$\tan(\phi_1) = \frac{[\sin(\theta) - \sin(\beta_1)]^2}{\sin(\theta - \beta_1)\sin(\beta_1)\sin(\theta)} \quad (2)$$

Eqs. (3)–(5) (see Fig. 15a).

The length of the C_2–Ut_o segment gives the slip along the ramp (S). The propagation of the upper ramp tip (P_u) is given by the Ut–Ut_o segment length. Bed thickness preservation imposes the following equation to be verified:

$$P_u\sin(\theta) = (P_u - S)\sin(\beta_2) \quad \text{(A9)}$$

The equation can also be written as:

$$\frac{S}{P_u} = 1 - \frac{\sin(\theta)}{\sin(\beta_2)} \quad (3)$$

or as:

$$\beta_2 = \arcsin(Q) \quad (4)$$

with

$$Q = \left[\frac{\sin(\theta)}{1 - \frac{S}{P_u}}\right] \quad (5)$$

Eq. (6) (see Fig. 15a).

The amount of excess layer-parallel shear at the stratigraphic elevation of Ut relates to both the ramp dip (θ) and the forelimb cutoff angle (β_2) through the following equations:

$$H\tan(\phi_1) + H(\beta_2 - \theta) + H\cot(\beta_2) = H\cot(\theta) \quad \text{(A10)}$$

simplifying:

$$\tan(\phi_u) = \cot(\theta) - \cot(\beta_2) + (\theta - \beta_2) \quad (6)$$

Eqs. (8) and (9) (see Fig. 15b).

The length of the C_2–Ut_0 segment gives the slip along the ramp (S). The propagation of the upper ramp tip (P_u) is given by the Ut–Ut_0 segment length. Bed thickness preservation imposes the following equation to be verified:

$$(P_u - S) = P_u\sin(\beta_3) \quad \text{(A11)}$$

The equation can also be written as:

$$\frac{S}{P_u} = 1 - \sin(\beta_3) \quad (8)$$

This equation can be written as:

$$\beta_3 = \arcsin\left[1 - \frac{S}{P_u}\right] \quad (9)$$

Eq. (10) (see Fig. 15b).

The amount of excess layer-parallel shear at the stratigraphic elevation of Ut relates to both the ramp dip (θ) and the syncline panel cutoff angle (β_3) through the following equations:

$$H\tan(\phi_1) + H\left(\frac{\pi}{2} - \theta\right) + (\mathrm{Ut} - T_2) = H\cot(\theta) + (T_1 - T_2) \quad \text{(A12)}$$

with:

$$\frac{(\mathrm{Ut} - T_2)}{\sin(\theta)} = \frac{(T_1 - T_2)}{\sin(\beta_3)} \quad \text{(A13)}$$

and with:

$$(\mathrm{Ut} - T_2) = H\left[\cot(\beta_3) - \cot\left(\frac{\theta + \beta_3}{2}\right)\right] \quad \text{(A14)}$$

Substituting Eqs. (A13) and (A14) into Eq. (A12) we obtain:

$$H\tan(\phi_1) + H\left(\frac{\pi}{2} - \theta\right) + H\left[\cot(\beta_3) - \cot\left(\frac{\theta + \beta_3}{2}\right)\right]\left[1 - \frac{\sin(\beta_3)}{\sin(\theta)}\right] = H\cot(\theta) \quad \text{(A15)}$$

By simplifying, the equation can also be written as:

$$\tan(\phi_1) = \cot(\theta) - \left(\frac{\pi}{2} - \theta\right) - \left[\frac{\sin\left(\frac{\theta-\beta_3}{2}\right)}{\sin\left(\frac{\theta+\beta_3}{2}\right)}\right]\left(\frac{1}{\sin(\beta_3)}\right)\left[\frac{\sin(\theta) - \sin(\beta_3)}{\sin(\theta)}\right] \quad \text{(A16)}$$

that can also be written as:

$$\tan(\phi_u) = \cot(\theta) - \left(\frac{\pi}{2} - \theta\right) - \left\{\frac{[\sin(\theta) - \sin(\beta_3)]^2}{\sin(\theta)\sin(\beta_3)\sin(\theta + \beta_3)}\right\} \quad (10)$$

Replacing circular sectors with kink-bands implies different line-length distributions. In particular the difference between line-length in a circular sector with respect to the corresponding kink-band is given by the following equation:

$$\text{Diff} = \upsilon - 2\tan\left(\frac{\upsilon}{2}\right) \tag{A17}$$

with υ being the circular sector apical angle. By applying this criterion, in the kink-style configuration Eq. (6) is replaced by:

$$\tan(\phi_u) = \cot(\theta) - \cot(\beta_2) - 2\tan\left(\frac{\theta-\beta_2}{2}\right) \tag{11}$$

Eq. (10) is replaced by:

$$\tan(\phi_u) = \cot(\theta) - 2\tan\left(\frac{\pi}{4}-\frac{\theta}{2}\right) - \left\{\frac{[\sin(\theta)-\sin(\beta_3)]^2}{\sin(\theta)\sin(\beta_3)\sin(\theta+\beta_3)}\right\} \tag{12}$$

References

Allmendinger, R., 1998. Inverse and forward numerical modelling of trishear fault-propagation folds. Tectonics 17, 640–656.

Alvarez, W., Engelder, T., Geiser, P., 1978. Classification of solution cleavage in pelagic limestones. Geology 6, 263–266.

Apotria, T., Wilkerson, M.S., 2002. Seismic expression and kinematics of a fault-related fold termination: Rosario structure, Maracaibo Basin, Venezuela. Journal of Structural Geology 24, 671–687.

Averbuch, O., Frizon de Lamotte, D., Kissel, C., 1992. Magnetic fabric as a structural indicator of the deformation path within a fold-thrust structure: a test case from the Corbières (NE Pyrenees, France). Journal of Structural Geology 14, 461–474.

Bally, A.W., Gordy, P.L., Stewart, G.A., 1966. Structure, seismic data, and orogenic evolution of southern Canadian Rocky Mountains. Bulletin of Canadian Petroleum Geology 14, 337–381.

Cartwright, J.A., Trudgill, B.D., Mansfield, C.S., 1995. Fault growth by segment linkage: an explanation for scatter in maximum displacement and trace length data from the Canyonlands Grabens of SE Utah. Journal of Structural Geology 17, 1319–1326.

Casas, J.M., Muñoz, J.A., 1987. Sequences of mesostructures related to the development of Alpine thrusts in the Eastern Pyrenees. Tectonophysics 135, 67–75.

Chester, J.S., 2003. Mechanical stratigraphy and fault–fold interaction, Absaroka thrust sheet, Salt River Range, Wyoming. Journal of Structural Geology 25, 1171–1192.

Chester, J.S., Chester, F.M., 1990. Fault-propagation folds above thrusts with constant dip. Journal of Structural Geology 12, 903–910.

Childs, C., Nicol, A., Walsh, J.J., Watterson, J., 1996. Growth of vertically segmented normal faults. Journal of Structural Geology 18, 1389–1397.

Corbett, K., Friedmean, M., Spang, J., 1987. Fracture development and mechanical stratigraphy of Austin Chalk, Texas. American Association of Petroleum Geologists Bulletin 71, 17–28.

Cristallini, E.O., Allmendinger, R.W., 2002. Backlimb trishear: a kinematic model for curved folds developed over angular fault bends. Journal of Structural Geology 24, 289–295.

Dahlstrom, C.D.A., 1969. Balanced cross-section. Canadian Journal of Sciences 6, 743–757.

Davis, E.E., Hyndman, R.D., 1989. Accretion and recent deformation of sediments along the northern Cascadia subduction zone. Geological Society of America Bulletin 101, 1465–1480.

Donath, F.A., Parker, R.B., 1964. Folds and folding. Geological Society of America Bulletin 75, 45–62.

Eisenstadt, G., De Paor, D.G., 1987. Alternative model of fault propagation. Geology 15, 630–633.

Elliott, D., 1976. The motion of thrust sheets. Journal of Geophysical Research 81, 949–963.

Ellis, M.A., Dunlap, W.J., 1988. Displacement variation along thrust faults: implications for the development of large faults. Journal of Structural Geology 10, 183–192.

Erslev, E.A., 1991. Trishear fault-propagation folding. Geology 19, 617–620.

Erslev, E.A., Mayborn, K.R., 1997. Multiple geometries and modes of fault-propagation folding in the Canadian thrust belt. Journal of Structural Geology 19, 321–335.

Faill, R.T., 1973. Kink band folding. Valley and Ridge province, Pennsylvania. Geological Society of America Bulletin 84, 1289–1314.

Fisher, D.M., Anastasio, D.J., 1994. Kinematic analysis of a large-scale leading edge fold, Lost River Range, Idaho. Journal of Structural Geology 16, 337–354.

Fischer, M.B., Jackson, P.B., 1999. Stratigraphic controls on deformation patterns in fault-related folds: a detachment fold example from the Sierra Madre Oriental, northeast Mexico. Journal of Structural Geology 21, 613–633.

Fischer, M.B., Woodward, N.B., Mitchell, M.M., 1992. The kinematics of break-thrust folds. Journal of Structural Geology 14, 451–460.

Flueh, E.R., Fisher, M.A., Bialas, J., Childs, J.R., Klaeschen, D., Kukowski, N., Parsons, T., Scholl, D.W., Brink, U., Tréhu, A.M., Vidal, N., 1998. New seismic images of the Cascadia subduction zone from cruise SO108—ORWELL. Tectonophysics 293, 69–84.

Gawthorpe, R.L., Sharp, I., Underhill, J.R., Gupta, S., 1997. Linked sequence, stratigraphic and structural evolution of propagating normal faults. Geology 25, 795–798.

Geiser, P.A., 1988. Mechanisms of thrust propagation: some examples and implications for the analysis of overthrust terranes. Journal of Structural Geology 10, 829–845.

Goff, D., Wiltschko, D.V., 1992. Stresses beneath a ramping thrust sheet. Journal of Structural Geology 14, 437–449.

Hamblin, W.K., 1965. Origin of 'reverse drag' on the downthrown side of normal faults. Geological Society of America Bulletin 76, 1145–1165.

Hardy, S., Ford, M., 1997. Numerical modeling of trishear fault propagation folding. Tectonics 16, 841–854.

Hardy, S., McClay, K., 1999. Kinematic modelling of extensional fault-propagation folding. Journal of Structural Geology 21, 695–702.

Hossack, J.R., 1979. The use of balanced cross-sections in the calculation of orogenic contraction: a review. Journal of the Geological Society of London 136, 705–711.

Jamison, W.R., 1987. Geometric analysis of fold development in overthrust terranes. Journal of Structural Geology 9, 207–219.

Jamison, W.R., 1992. Stress controls of fold thrust style. In: McClay, K.R. (Ed.), Thrust Tectonics. Chapman and Hall, London, pp. 155–164.

Jordan, P., Noack, T., 1992. Hanging wall geometry of overthrust emanating from ductile decollements. In: McClay, K.R. (Ed.), Thrust Tectonics. Chapman and Hall, London, pp. 311–318.

Julivert, M., Arboleya, M., 1984. A geometrical and kinematical approach to the nappe structure in an arcuate fold belt: the Cantabrian nappes (Hercynian chain, NW Spain). Journal of Structural Geology 6, 449–519.

Liu, S., Dixon, J.M., 1995. Localization of duplex thrust-ramps by buckling: analog and numerical modelling. Journal of Structural Geology 17, 875–886.

Marshak, S., Engelder, T., 1985. Development of cleavage in limestones of a fold-trust belt in eastern New York. Journal of Structural Geology 7, 345–359.

McConnel, D.A., Kattenhorn, S.A., Benner, L., 1997. Distribution of fault slip in outcrop-scale fault-related folds, Appalachian mountains. Journal of Structural Geology 19, 257–267.

McNaught, M.A., Mitra, G., 1993. A kinematic model for the origin if footwall synclines. Journal of Structural Geology 15, 805–808.

Medwedeff, D.A., 1992. Geometry and kinematics of an active, laterally

propagating wedge thrust, Wheeler Ridge, California. In: Mitra, S., Fisher, S. (Eds.), Structural Geology of Fold and Thrust Belts. John Hopkins University Press, Baltimore, pp. 3–28.

Mercier, E., Outtani, F., Frizon De Lamotte, D., 1997. The late evolution of fault-propagation folds: principles and example. Journal of Structural Geology 19, 185–193.

Mitra, G., Yonkee, W.A., 1985. Relationship of spaced cleavage to folds and thrusts in the Idaho–Utah–Wyoming thrust belt. Journal of Structural Geology 7, 361–373.

Mitra, S., 1990. Fault-propagation folds: geometry, kinematic evolution, and hydrocarbon traps. American Association of Petroleum Geology Bulletin 74, 921–945.

Mitra, S., 2002. Fold accommodation faults. American Association of Petroleum Geology Bulletin 86, 1673–1694.

Mitra, S., 2003. A unified kinematic model for the evolution of detachment folds. Journal of Structural Geology 25, 1659–1673.

Moore, G.F., Shipley, T.H., Stoffa, P.L., Karig, D.E., Taire, A., Kuramoto, S., Tokuyama, H., Suyehiro, K., 1990. Structure of the Nankai Trough accretionary zone from multichannel seismic reflection data. Journal of Geophysical Research 95, 8753–8766.

Morgan, J.K., Karig, D.E., 1995. Kinematics and balanced cross-section across the toe of the eastern Nankai accretionary prism. Journal of Structural Geology 17, 31–45.

Morley, C.K., 1994. Fold-generated imbricates: examples from the Caledonides of Southern Norway. Journal of Structural Geology 16, 619–631.

Mosar, J., Suppe, J., 1992. Role of shear in fault-propagation folding. In: McClay, K.R. (Ed.), Thrust Tectonics. Chapman and Hall, London, pp. 123–132.

Mueller, K., Suppe, J., 1997. Growth of Wheeler Ridge anticline, California: geomorphic evidence for fault-bend folding behaviour during eartquakes. Journal of Structural Geology 19, 383–396.

Muroaka, H., Kamata, H., 1983. Displacement distribution along minor fault traces. Journal of Structural Geology 5, 395–483.

Price, R.A., 1988. The mechanical paradox of large overthrusts. Geological Society of America Bulletin, v 100, 1898–1908.

Ramsay, J.G., 1974. Development of chevron folds. Geological Society of America Bulletin 85, 1741–1754.

Rich, J.L., 1934. Mechanics of low-angle overthrust faulting as illustrated by the Cumberland Thrust Block, Virginia, Kentucky and Tennessee. American Association of Petroleum Geologists Bulletin 18, 1584–1596.

Rutter, E.H., 1983. Pressure solution in nature, theory and experiment. Journal of the Geological Society of London 140, 725–740.

Sans, M., Vergés, J., Gomis, E., Parés, J.M., Schiattarella, M., Travé, A., Calvet, F., Santanach, P., Doulcet, A., 2003. Layer parallel shortening in salt-detached folds: constraint on cross-section restoration. Tectonophysics 372, 85–104.

Srivastava, D.C., Engelder, T., 1990. Crack-propagation sequence and pore-fluid conditions during fault-bend folding in the Appalachian Valley and Ridge, central Pennsylvania. Geological Society of America Bulletin 102, 116–128.

Storti, F., Salvini, F., McClay, K., 1997. Fault-related folding in sandbox analogue models of thrust wedges. Journal of Structural Geology 19, 583–602.

Storti, F., Tavani, S., Moscardini, F., Merlini, S., Salvini, F., 2004. The Basil anticline. In: Shaw, J.H., Connors, C., Suppe, J. (Eds.), Seismic Interpretation of Contractional Fault-related Folds: An AAPG Seismic Atlas. AAPG Special Publication.

Suppe, J., 1983. Geometry and kinematics of fault-bend folding. American Journal of Sciences 283, 684–721.

Suppe, J., 1985. Principles of Structural Geology. Prentice-Hall, Englewood Cliffs, NJ.

Suppe, J., Medwedeff, D.A., 1984. Fault-propagation folding. Geological Society of America Bulletin, Abstracts with Programs 16, 670.

Suppe, J., Medwedeff, D.A., 1990. Geometry and kinematics of fault-propagation folding. Ecoglae Geologicae Helvetiae 83, 409–454.

Suppe, J., Chou, G.T., Hook, S.C., 1992. Rates of folding and faulting determined from growth strata. In: McClay, K.R. (Ed.), Thrust Tectonics. Chapman and Hall, London, pp. 105–121.

Suppe, J., Connors, C.D., Zhang, Y., 2004. Shear fault-bend folding. In: McClay, K.R. (Ed.), Thrust Tectonics and Petroleum Systems. American Association of Petroleum Geologists Memoirs, 82, pp. 303–323.

Tavani, S., Storti, F., Salvini, F., 2005. Rounding hinges to fault-bend folding: geometric and kinematic implications. Journal of Structural Geology 27, 3–22.

Walsh, J.J., Watterson, J., 1988. Analysis of the relationship between the displacements and dimensions of faults. Journal of Structural Geology 10, 239–247.

Wickham, J., 1995. Fault displacement-gradient folds and the structure at Lost Hills, California (USA). Journal of Structural Geology 17, 1293–1302.

Williams, G.D., Chapman, T.J., 1983. Strains developed in the hanging walls of thrust due to their slip/propagation rate: a dislocation model. Journal of Structural Geology 6, 563–571.

Willis, B., 1893. The mechanics of Appalachian structures. US Geological Survey Annual Report 13 (1891–1892), part. 2, pp. 217–281.

Woodward, N.B., Boyer, S.E., Suppe, J., 1989. Balanced geological cross-section: an essential technique in geological research and exploration. American Geophysical Union Short Course in Geology 6.

Xiao, H., Suppe, J., 1992. Origin of rollover. American Association of Petroleum Geologists Bulletin 76, 509–529.

Zehnder, A.T., Allmendinger, R.W., 2002. Velocity field for the trishear model. Journal of Structural Geology 22, 1009–1014.